

# Strategies for Volumetric Recovery of Large Scale Damage in Polymers

Brett P. Krull, Ryan C. R. Gergely, Windy A. Santa Cruz, Yelizaveta I. Fedonina, Jason F. Patrick, Scott R. White, and Nancy R. Sottos\*

The maximum volume that can be restored after catastrophic damage in a newly developed regenerative polymer system is explored for various mixing, surface wetting, specimen configuration, and microvascular delivery conditions. A two-stage healing agent is implemented to overcome limitations imposed by surface tension and gravity on liquid retention within a damage volume. The healing agent is formulated as a two-part system in which the two reagent solutions are delivered to a through-thickness, cylindrical defect geometry by parallel microvascular channels in thin epoxy sheets. Mixing occurs as the solutions enter the damage region, inducing gelation to initiate an accretive deposition process that enables large damage volume regeneration. The progression of the damage recovery process is tracked using optical and fluorescent imaging, and the mixing efficiency is analyzed. Complete recovery of gaps spanning 11.2 mm in diameter (98 mm<sup>2</sup>) is achieved under optimal conditions.

## 1. Introduction

Although autonomous repair of injured tissue is commonplace in biological systems, synthetic materials remain susceptible to damage. Recent advances in self-healing material systems

Dr. B. P. Krull, Y. I. Fedonina, Prof. N. R. Sottos  
Department of Materials Science and Engineering  
Beckman Institute for Advanced Science and  
Technology  
University of Illinois at Urbana-Champaign  
Urbana, IL 61801, USA  
E-mail: n-sottos@illinois.edu

R. C. R. Gergely  
Department of Mechanical Science and Engineering  
Beckman Institute for Advanced Science and Technology  
University of Illinois at Urbana-Champaign  
Urbana, IL 61801, USA

Dr. W. A. Santa Cruz  
Department of Chemistry  
Beckman Institute for Advanced Science and Technology  
University of Illinois at Urbana-Champaign  
Urbana, IL 61801, USA

Dr. J. F. Patrick  
Beckman Institute for Advanced Science and Technology  
University of Illinois at Urbana-Champaign  
Urbana, IL 61801, USA

Prof. S. R. White  
Department of Aerospace Engineering  
Beckman Institute for Advanced Science and Technology  
University of Illinois at Urbana-Champaign  
Urbana, IL 61801, USA

DOI: 10.1002/adfm.201600486



promise to improve safety and extend the lifetime of components in a variety of applications ranging from aerospace to microelectronics.<sup>[1–5]</sup> Most prior work in this field focuses on recovering mechanical or fracture properties for materials containing cracks of width less than 100 μm; however, catastrophic damage events that remove mass or create millimeter-scale crack separations require new self-healing strategies.<sup>[6]</sup>

Blaiszik et al.<sup>[7]</sup> identified three major categories of self-healing materials: intrinsic, capsule-based, and vascular. Intrinsic self-healing materials possess reversible chemical functionalities (i.e., ionic or hydrogen bonding) which break during a damage event and reform to

facilitate healing. Intrinsic self-healing materials are unable to repair large crack separations because healing occurs on the molecular level and requires intimate contact.<sup>[8,9]</sup> In contrast, capsule-based approaches may tolerate small crack separations. Fluid-filled spheres are embedded into a material and the encapsulated liquids, or healing agents, consist of monomers or other reactive chemical species. When a fracture event occurs, the crack will traverse the material and intersect the embedded capsules to release a liquid payload. The healing agents fill the damage zone and polymerize to rebond the crack planes and arrest further crack propagation. Restrictions on capsule size and concentration limit the total volume of healing agents available for delivery, and thus, limit the maximum crack separation that can be repaired.<sup>[10,11]</sup>

Vascular self-healing systems are synthetic materials with embedded biomimetic microvascular networks that circulate a continuous supply of liquid healing agents.<sup>[11–20]</sup> As a damage event occurs, cracks intersect the vascular network to release healing agents. Despite occupying a very a low proportion of the total material volume (≈0.50 vol% for a pervasive network),<sup>[20]</sup> vasculature can supply a virtually limitless quantity of healing agents from a reservoir external to the material system. Therefore, microvascular self-healing materials are capable of the mass transport necessary to address large damage volumes, but new materials are required to regenerate functional structures (i.e., achieve volumetric recovery) rather than simply rebond crack planes or repair surfaces.<sup>[21]</sup> For example, Yong et al. report on computational analysis of a gel matrix that regrows after a significant portion is severed<sup>[22]</sup> and Zavada et al. demonstrate repair of ballistic impact on resin-filled panels using

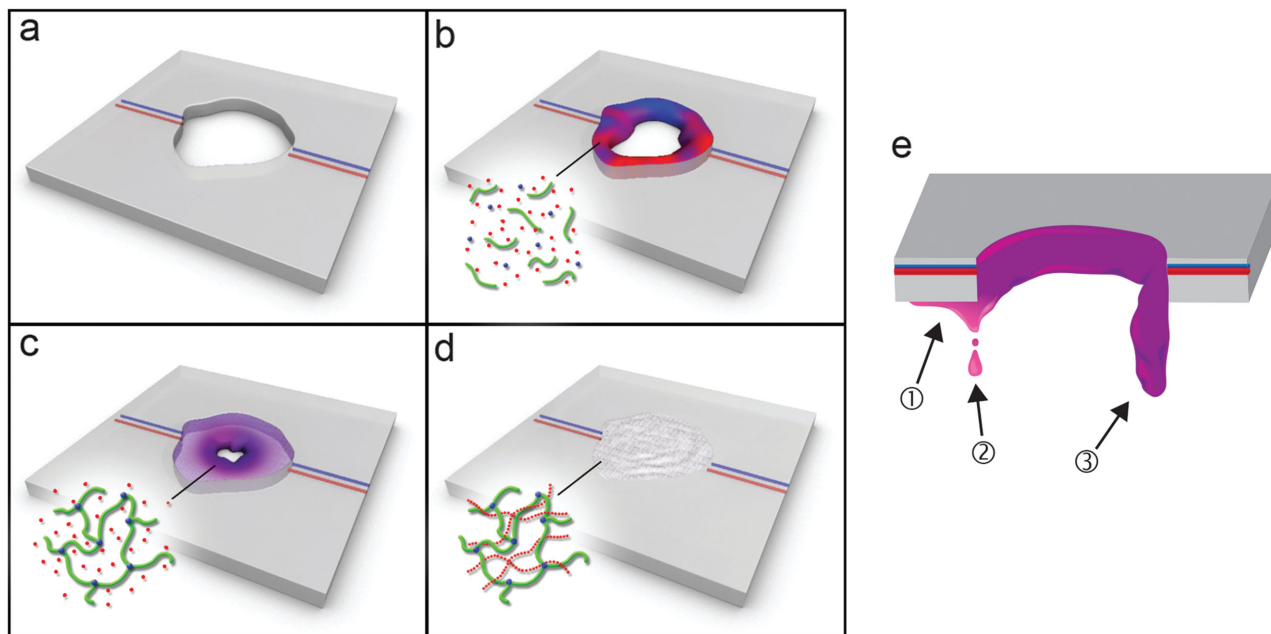


**Figure 1.** Schematic showing the regenerative healing process for a two-stage healing agent system. a) A damage event causes loss of mass in the microvascular material. b) Two-part chemical healing system is released into the damage volume where mixing occurs. Green segments represent gelator A [PEG-based oligomer], blue dots represent gelator B [aldehyde crosslinker] and the red dots represent the monomer solvent. (Composition given in Figure S1 and Table S1, Supporting Information). c) Gelation occurs rapidly via acid-catalyzed reaction of the dissolved gelators. d) Polymerization of the monomer solvent into a structural material. e) Failure modes observed during the fill process: ① surface wetting; ② ungelled reagent dripping; and ③ deflection of the gel.

an environment-initiated thiol-ene healing agent chemistry that rapidly sealed single-sided puncture damage of 1–2 mm diameter.<sup>[23]</sup>

Recently, White et al. introduced a two-stage polymer system capable of restoring open damage volumes.<sup>[24]</sup> The large damage volume recovery process is illustrated in **Figure 1**. The two-stage polymer was separated into two stable reagent solutions and isolated into adjacent microvascular networks. When damage occurred, the vasculature was ruptured, causing the solutions to mix (Figure 1a,b) and initiating two simultaneous chemical reactions. First, a rapid gelation ( $\approx 30$  s, Figure 1c) occurred via the acid-catalyzed reaction of gelator A (bis-acylhydrazine-terminated poly(ethylene glycol)) and gelator B (tris[4-(4-formylphenoxy)methyl]ethane) to create a crosslinked network containing the liquid monomer solvent (2-hydroxyethylmethacrylate, HEMA). Subsequently, room temperature polymerization of the HEMA was achieved via promoted free-radical initiation using methyl ethyl ketone peroxide and cobalt naphthenate to form a rigid solid ( $>1$  h, Figure 1d). The gelation of the two-stage polymer enabled the recovery of large damage volumes. Without formation of the gel, liquids remained mobile and susceptible to external forces that caused the healing agents to flow out from the large, open damage regions.

White et al. reported a 104% increase for maximum damage area recovered in a through-thickness cylindrical defect geometry for a gelling healing chemistry compared to a neat HEMA control that did not gel.<sup>[24]</sup> Beyond a 9.0 mm damage diameter, samples only partially filled due to three failure modes illustrated in Figure 1e. First, wetting of the healing agents on either the top or bottom surface of the sample wicked

un-gelled healing agents out of the damage volume by capillary forces (①). Second, excessive gel formation inhibited microvascular delivery of the solution containing the acid catalyst, preventing further gelation of the system. Without gelation, the components of the two-stage chemistry bled out from the damage volume (②). Finally, the growing gel mass on occasion deflected downward rather than closing the gap in the center of the damage volume (③). White et al. reported results for a single test protocol and the influence of experimental variables on these failure modes was not explored.

Here, we investigate the effects of the two-stage healing agent delivery schedule, sample configuration, healing agent contact angle, and number of microvascular channels on the maximum fill size of cylindrical defect geometries in thin epoxy sheets using the HEMA-based regenerative healing chemistry (composition Figure S1, Table S1, Supporting Information) previously introduced by White et al.<sup>[24]</sup> By altering experimental conditions, we extend the maximum repair diameter to 11.2 mm (197% increase over the neat HEMA control) for our regenerative polymer system.

## 2. Results and Discussion

### 2.1. Progression of Damage Recovery

The progression of damage recovery was examined for vascular delivery of healing agents to an ideal cylindrical damage geometry. The behavior of a HEMA gel healing agent chemistry (Figure S1, Table S1, Supporting Information) differs markedly

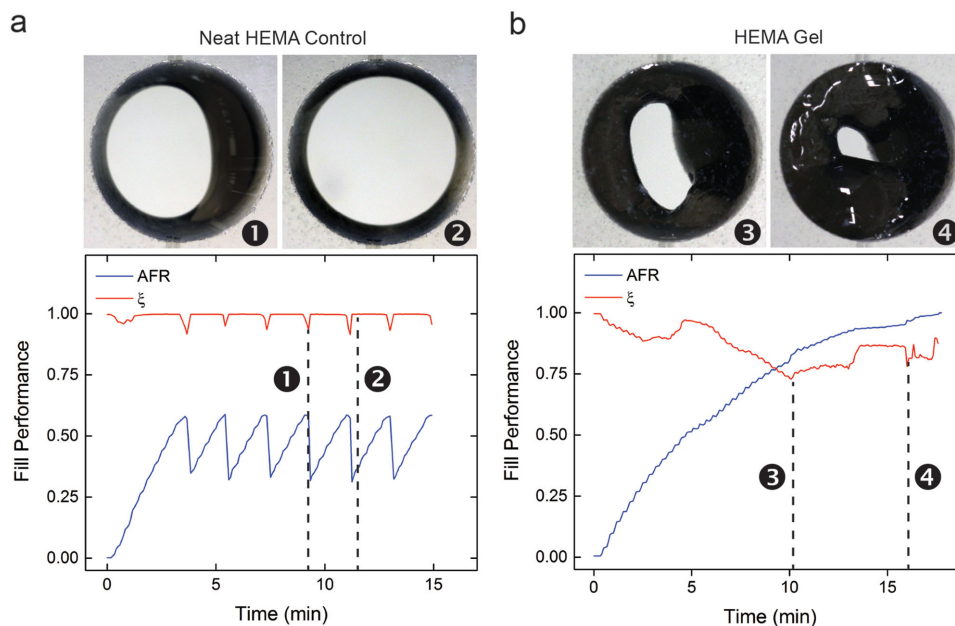


**Figure 2.** Progression of damage recovery with AFR and degree of circularity ( $\xi$ ) for a) neat HEMA control and b) HEMA gel. Damage diameter is 7.0 mm. (①–④) depict the time at which the image and corresponding graphical data were collected. HEMA gel and control solutions each contain 0.0001 wt% carbon black for contrast enhancement.

from that of a neat HEMA control (non-gelling). We recorded the progression of damage recovery as a function of time in a series of overhead images (Figure 2). Fill progress was assessed by defining an Area fill ratio (AFR)

$$\text{AFR} = \frac{A_{\text{fill}}}{A_0} \quad (1)$$

where  $A_{\text{fill}}$  is the damage area recovered by healing agents as viewed from above and  $A_0$  is total area of the original cylindrical damage zone. Carbon black (Regal 400, Cabot) was added at 0.0001 wt% to improve contrast of the healing agent for optical analysis. AFR data for the neat HEMA control and the HEMA gel system are shown in Figure 2a,b (blue lines), respectively. The neat HEMA control repeatedly reached an AFR of  $\approx 0.59$  before gravity pulled the healing agents from the damage volume and reduced the AFR to  $\approx 0.33$ . In contrast, the gel followed a steady progression toward a complete fill of the damage area. This result demonstrates the ability of the two-stage chemistry to recover large damage volumes through the formation of a dynamic gel network.<sup>[25]</sup>

For the cylindrical damage geometry, liquid healing agents appeared as an annulus when viewed from above with an open, circular area present in the center of the damage region. The extent to which the healing agents conformed to a circular contour was calculated from the shape of the unfilled portion of the damage geometry<sup>[26]</sup>

$$\xi = 1 - \frac{1}{R_0} \sqrt{\frac{\sum_{i=1}^N [(x_i - A_0)^2 + (y_i - B_0)^2 - R_0^2]^2}{4R_0^2 N \left(1 - \frac{3}{N}\right)^2}} \quad (2)$$

where  $\xi$  is the degree of circularity,  $x_i$  and  $y_i$  are the coordinates of points around the contour of the unfilled portion of the damage geometry,  $A_0$  and  $B_0$  are the center coordinates of a best fit circle calculated for the unfilled portion of the damage geometry,  $R_0$  is the radius of the best fit circle, and  $N$  is the number of points used to construct the best fit circle. When the outline of the healing agent approached that of a perfect circle, then  $\xi = 1$ .

Figure 2a,b (red lines) show  $\xi$  for the neat HEMA control and HEMA gel system, respectively. The fill shape of the control fluid is dictated by surface tension, appearing circular in shape until immediately preceding a drip when gravity dominates and pulls the liquid from the damage zone. In great contrast, the gel material deviates significantly from circularity at the onset of the test and follows no predictable trend, indicating the shape of the gel is not dominated by surface tension alone (Movies S1 and S2, Supporting Information).

## 2.2. Effect of Mixing

Delivery schedule was varied for regeneration experiments to gauge the effect on mixing and maximum fill size. Three pumping protocols were prescribed to alter the cadence of flow while maintaining the overall cycle time and average delivery rate of previously reported fill results.<sup>[24]</sup> White et al. developed an alternating delivery scheme of: 1 s pulsed delivery of 1  $\mu\text{L}$  solution B, 3 s delay, 1 s pulsed delivery of 1  $\mu\text{L}$  solution A, and a 15 s delay for a total cycle time of 20 s. Two additional pumping protocols were examined for comparison (Figure S2, Supporting Information). The first was a simultaneous pumping schedule, which delivered solutions concurrently. The second was a double-frequency alternating schedule with 4 alternating pulses each of 0.5  $\mu\text{L}$  volume.

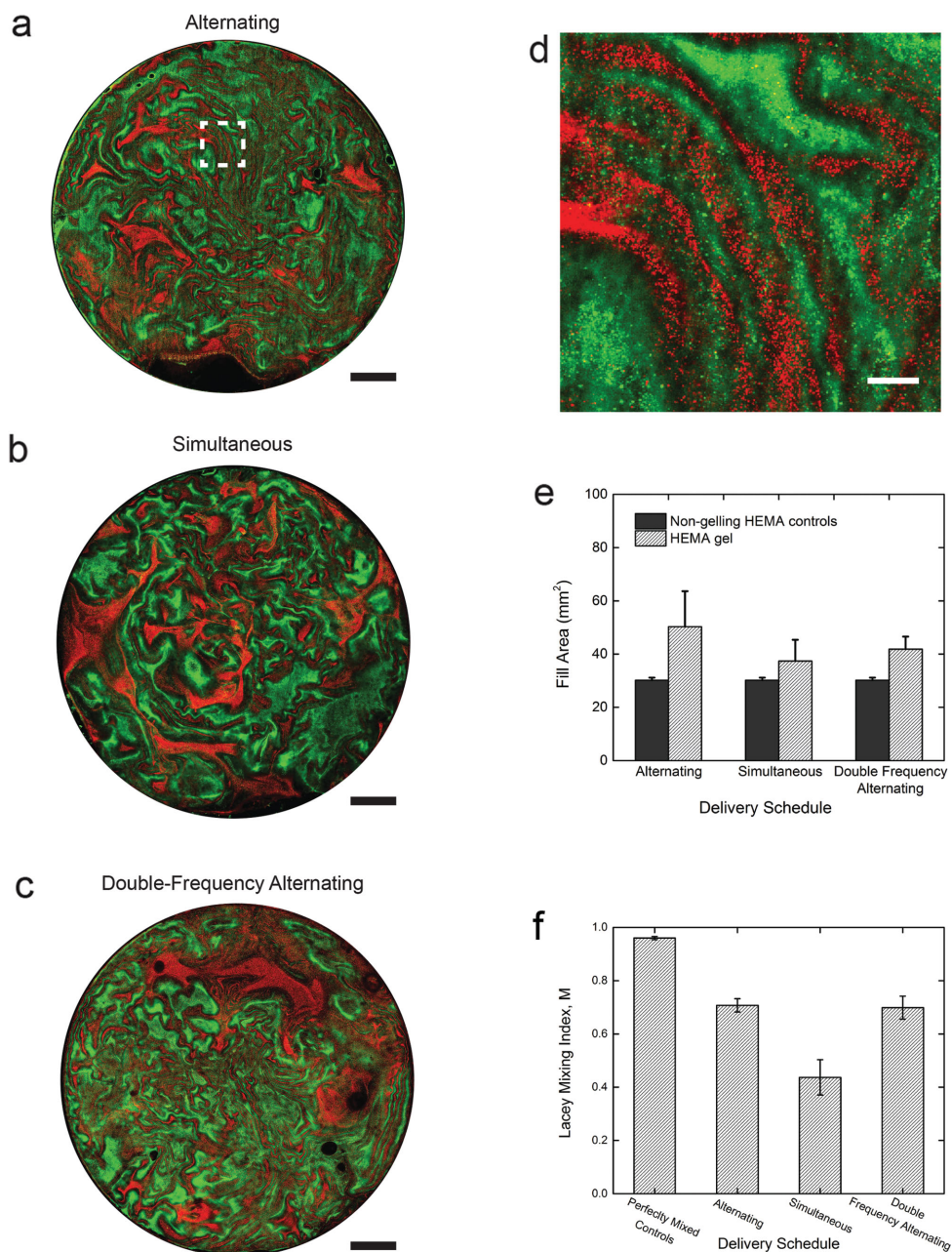


**Figure 3.** Effects of fluid delivery and mixing. Micrograph from scanning laser confocal microscope showing a distribution of fluorescent nanoparticles (red=rhodamine B; green=fluorescein) for a representative sample of each delivery schedule a) alternating flow b) simultaneous flow, and c) double-frequency alternating flow (scale bars = 1 mm, damage diameter = 6.5 mm). d) Higher magnification region indicated by white box in (a) (scale bar = 100  $\mu$ m). e) Fill performance of various delivery schedules. f) Lacey mixing index (Equation (3)) of perfectly mixed samples and each delivery schedule.

Confocal fluorescence microscopy was used to analyze the position of fluorescent dyed nanoparticles, dispersed in the healing agents, to gain a direct indication of mixing. Fluorescent silica nanoparticles ( $\approx 300$  nm) containing either rhodamine B or fluorescein were synthesized<sup>[27,28]</sup> and suspended in each of the healing agent components (rhodamine—Part A, fluorescein—Part B). As the two-part system mixed during delivery, gelation locked the nanoparticles in place and the nanoparticle silica shells prevented the dyes from diffusing during a 24 h cure process. After allowing the healing chemistry to

fully cure into a rigid polymer, confocal micrographs of polished surfaces showed a striated appearance with notable concentrations of each nanoparticle species (Figure 3a–d, all test replicates shown in Figure S3, Supporting Information). The striated appearance of the fluorescent nanoparticles is indicative of accretion of the gel mass and provided an opportunity for quantifying the extent of mixing.

We evaluated the distribution of the dyed nanoparticles by converting each channel into a binary image (see Section 4), overlaying a  $30 \times 30$  cell grid (cell size  $\approx 200 \mu\text{m} \times 200 \mu\text{m}$ ), and

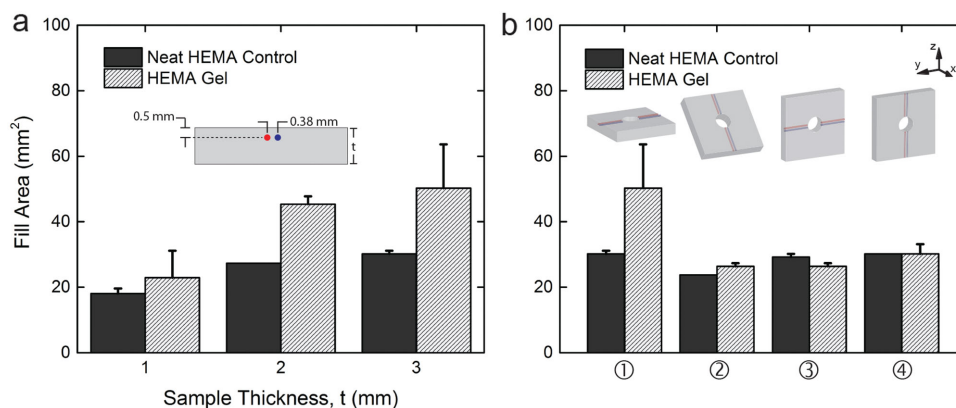


**Figure 4.** Effect of thickness and orientation on fill performance. a) Fill area of neat HEMA control and HEMA gel for each sample thickness. b) Fill area of samples with following orientations: ① 0°, ② 45° vertical channels, ③ 90° horizontal channels, ④ 90° vertical channels.

calculating cell concentrations of each dye via MATLAB pixel count. Lacey described a statistical method to determine the degree of mixing between two particulate species<sup>[29]</sup>

$$M = \frac{\sigma_0^2 - \sigma^2}{\sigma_0^2 - \sigma_R^2} \quad (3)$$

where  $M$  is the Lacey Mixing Index,  $\sigma_0$  is standard deviation of cell concentration in a completely unmixed sample,  $\sigma$  is the standard deviation of cell concentration in the actual sample, and  $\sigma_R$  is the standard deviation of cell concentration in a perfectly mixed sample.  $M$  approaches unity for a perfectly mixed sample. In this experimental setup, the pixels from confocal micrographs representing dyed nanoparticles are analogous to particulates investigated by Lacey. As opposed to other methods that rely on circumstantial evidence of mixing derived from mechanical data,<sup>[13,18,20]</sup> our analysis gives a direct assessment of healing agent mixing.

In all three delivery schedules, the gel filled a larger area than the control. The original alternating delivery schedule demonstrated the highest fill performance followed by the double-frequency alternating schedule and finally, the simultaneous delivery schedule (Figure 3e). In agreement with fill performance, the simultaneous delivery schedule showed the lowest degree of mixing (Figure 3f). However, alternating and double-frequency alternating schedules showed similar degrees of mixing despite differences in fill performance. Samples that were premixed with a vortex mixer (“perfectly mixed”) and manually injected into damage volumes yielded a mixing index,  $M$ , close to unity as expected.

We observed the healing chemistry is greatly affected by the stoichiometric ratio of the solutions (Table S2, Supporting Information). Although each of the schedules was calibrated to deliver 1:1 ratios of solutions, the local stoichiometry of a poorly mixed sample likely impacted gel time and regeneration performance. Degree of mixing influences fill size, but additional analysis is needed to better understand the extent to which mixing modifies influential factors such as the local viscosity or dynamic contact angle of healing agent and how these properties affect delivery and flow in the damage volume.

### 2.3. Sample Configuration

We investigated the effects of substrate thickness and sample orientation on maximum fill size to determine whether the surface area available for gel accretion or the direction of gravity would influence regeneration performance. The effect of sample thickness on maximum fill area is shown in Figure 4a. Sample thickness is varied from 1–3 mm while holding micro-channel position constant with respect to the upper surface. Increasing sample thickness resulted in an increased fill size for both the neat HEMA control and HEMA gel healing agents. Improved performance with increasing thickness was expected since the greater sample thicknesses provided a larger surface area to which healing agents may deposit, spread, and gel. The effect of thickness on fill size was more progressive for HEMA gel healing agents than with the neat HEMA control. The control experienced only a marginal benefit from thicker samples because gravity still limited retention of the non-gelling fluids.

The fill performance of the gelling healing agents under different damage orientations was investigated to better understand the effect of gravity on the healing process. Figure 4b shows the fill performance of the neat HEMA control and HEMA gel healing agents in four different sample orientations: ① 0°, ② 45° tilt with vertical channels, ③ 90° with horizontal channels, and ④ 90° with vertical channels. The 0° orientation reported in our previous study<sup>[24]</sup> far outperformed all other orientations for the gel. The control was largely unaffected by damage orientation. The gel only provided a marginal benefit over the control for the 45° tilt with vertical channels and 90° with horizontal channels. The control slightly outperformed the gel for the 90° with vertical channels test case.

In all orientations other than the 0° case, healing agents pooled at the bottom of the damage geometry, only covering a relatively small portion of the damage circumference. The pooling healing agents covered and blocking delivery from one or more of the channels due to formation of the gel. Consequently, the blockage resulted in poor mixing and/or inadequate ratios of components delivered to the damage region, which in turn decreased fill performance. In the 0° orientation, liquids were distributed and retained around the entire circumference of the damage zone and unencumbered flow was attained due to the position of

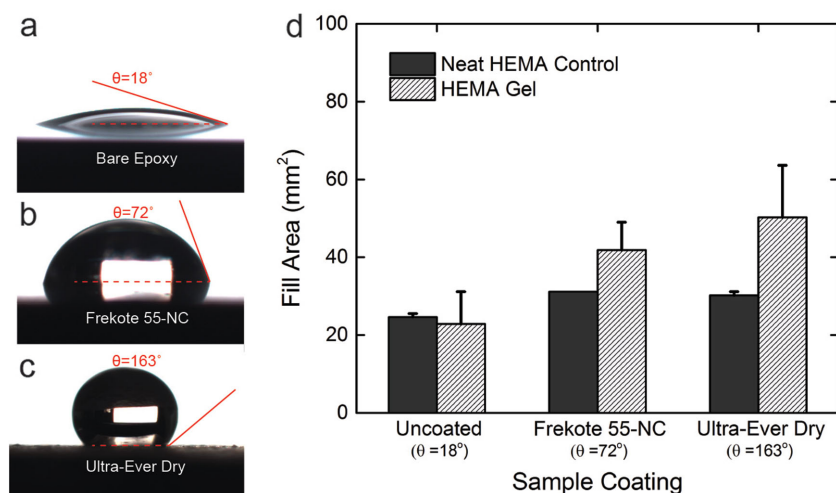


**Figure 5.** Effect of surface coating on wetting and fill performance. a) Contact angle of HEMA on uncoated epoxy, b) Frekote 55-NC, and c) Ultra-Ever Dry. d) Fill performance of samples with different surface coatings.

microchannels. Healing agents with faster gel times could potentially mitigate orientation challenges if gelation occurred before gravity draws healing agents to the lowest surface of the damage volume. The introduction of additional channels may also help the system resist failure due to channel blockage by ensuring channels at multiple orientations are present. Multiple channel orientations would provide a greater chance at least one channel of each type could remain unblocked by accumulating gel.

## 2.4. Surface Wetting

We investigated the effect of specimen coatings on the maximum damage fill size by delaying or preventing the surface wetting failure mode. The contact angle of HEMA is  $\theta = 18^\circ$  on untreated epoxy, near oleophobic ( $\theta = 72^\circ$ ) for Frekote NC-55, and superoleophobic ( $\theta = 163^\circ$ ) for Ultra-Ever Dry (UED) coated samples, respectively (Figure 5a–c). The tendency for liquids to traverse edges and wet adjacent surfaces is described by the Gibbs inequality condition<sup>[30]</sup>

$$\theta_1 \leq \theta_0 \leq (180 - \phi) + \theta_2 \quad (4)$$

where  $\theta_1$  is the equilibrium contact angle of the wetted surface,  $\theta_0$  is the contact angle of a liquid pinned at an edge,

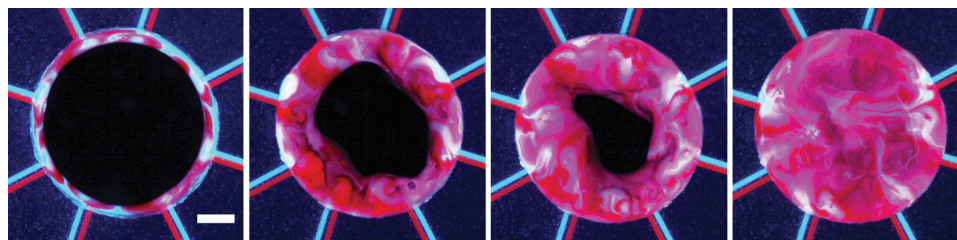


**Figure 6.** Fill progression for an 8-channel sample after 1, 5, 8, and 10 min into the fill process as viewed from above. Damage diameter is 10.5 mm (scale bar = 2 mm). Blue fluid is in Part A with 1.25 mg mL<sup>-1</sup> perylene dye. Red fluid is Part B with 0.6 mg mL<sup>-1</sup> DFWB-K10-50 and 1.5 mg mL<sup>-1</sup> Nile Red dyes. See Table S1 in the Supporting Information for details on solution compositions.

$\phi$  is the angle between the two surfaces, and  $\theta_2$  is the equilibrium contact angle of the non-wetted surface. For our experiments,  $\theta_1$  represents the damage surface and  $\theta_2$  represents the bottom and top surfaces of the sample (Figure S4, Supporting Information).  $\theta_1$  is  $18^\circ$  for all samples because damage exposes bare epoxy and  $\phi$  is  $90^\circ$  because damage is created perpendicular to the channels. However,  $\theta_2$  varies according to surface coating.

Figure 5d compares the fill performance for each coating condition. Bare epoxy samples were prone to wetting failure for both the neat HEMA control and gelling healing agents, resulting in only a marginal performance increase for the HEMA gel compared to the control. Healing agents often wetted the bottom surface of the sample prior to gelation. Both Frekote and UED coated samples achieved equivalent fill results for control liquids because the coatings eliminated the wetting failure mode. In contrast, the fill performance of the HEMA gel healing agents was much greater for the higher contact angle coating (UED). Gel buildup around the microchannels was observed to deflect flow onto both the top and bottom surfaces of the samples, where wetting was occasionally observed with Frekote but prevented by the higher contact angle UED. Changes in fill performance with respect to contact angle demonstrate the selective phobicity of the epoxy surface can be designed to alter the wetting of the healing agents<sup>[31,32]</sup> to attain greater fluid retention and volumetric recovery.

## 2.5. Concentration of Vascular Channels

Samples with 2, 4, and 8 intersecting channels were fabricated and evaluated for fill performance. Cylindrical damage volumes were created at the intersection of the channels (the damage event split each channel in half; e.g., the 2-channel specimens had 4 half-channels delivering fluids) and the healing agent delivery rate was held at 3  $\mu\text{L min}^{-1}$  per channel for each experimental configuration. Effectively, the overall volumetric flow rate of the healing agents increases proportionately with the number of channels. Figure 6 shows an image sequence of the fill process for an 8-channel specimen with a 10.5 mm damage diameter. We observed improved deposition with higher microvascular

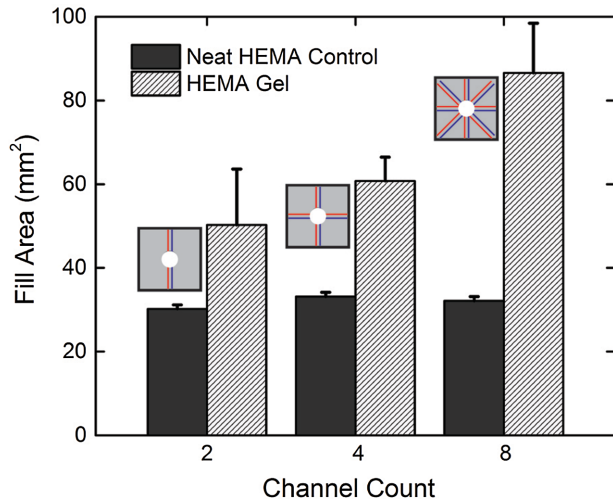


**Figure 7.** Effect of number of delivery channels on fill performance.

concentration, leading to enhanced regeneration performance (Figure 7). The maximum fill size of the control was largely unchanged by increasing the number of channels, but the 8-channel specimens attained greater fill sizes, reaching 164% improvement (11.2 mm damage diameter) in fill area over the original 2-channel sample geometry previously reported<sup>[24]</sup> and a 197% improvement of damage area recovered over the control.

## 2.6. Summary of Fill Performance

The HEMA gel system provides a versatile platform to address large damage volumes as demonstrated by the superior fill results compared to a neat HEMA control. Table 1 contains numerical values comparing the relative performance of all test

conditions. The fill performance was evaluated by calculating the fill factor as

$$\zeta = \frac{\alpha_{\text{gel}} - \alpha_{\text{control}}}{\alpha_{\text{control}}} \quad (5)$$

where  $\zeta$  is the fill factor,  $\alpha_{\text{gel}}$  is the maximum fill size attained by HEMA gel for a given experimental protocol (delivery schedule, sample geometry, sample orientation, surface coating, and microvascular density), and  $\alpha_{\text{control}}$  is the maximum fill size attained by the neat HEMA control for the same protocol. The gel outperformed the neat HEMA control fluids for every test case ( $\zeta > 0$ ) except for the 90° oriented test configuration with horizontal channel positioning ( $\zeta = -0.09$ ) which experienced severe channel blockage due to sample orientation. The performance is greatest for samples with an alternating pumping schedule, largest thickness, 0° orientation, superoleophobic surfaces, and highest concentration of microvascular channels. Under these conditions, the HEMA gel exceeded the maximum fill size of neat HEMA by a margin of 3:1.

## 3. Conclusion

The performance of a regenerative microvascular system was examined for a two-stage polymer healing agent by measuring the maximum size that could be filled for a cylindrical hole (damage) geometry while varying experimental conditions. Gelation was demonstrated to improve the ability of healing agents to fill large damage volumes by better resisting the effects of gravity and surface tension compared to non-gelling liquid healing agents. Under ideal test conditions, we achieved complete filling of a cylindrical through-thickness damage geometry 98.5 mm<sup>2</sup> in area (11.2 mm diameter). Mixing, wetting behavior, and microvascular density were shown to hold the greatest influence on

**Table 1.** Summary of maximum fill size attained for each test condition.

		Neat HEMA control		HEMA gel		Fill factor $\zeta$
		Diameter (mm)	Area (mm <sup>2</sup> )	Diameter (mm <sup>2</sup> )	Area (mm <sup>2</sup> )	
Standard specimen <sup>a)</sup>	(alternating delivery, 3 mm thickness, 0° orientation, $\theta = 163^\circ$ coating, 2 channels)	6.3	31.2	9.0	63.6	1.04
Experimental series <sup>b)</sup>	Variables					
Delivery schedule	Simultaneous	6.2	30.2	7.6	45.3	0.50
	Double-frequency alternating	6.3	31.2	7.7	46.5	0.49
Thickness	1 mm	5.0	19.6	6.3	31.2	0.59
	2 mm	5.9	27.3	7.8	47.8	0.75
Orientation	45°, Vertical channels	5.5	23.7	5.9	27.3	0.15
	90°, Horizontal channels	6.2	30.2	5.9	27.3	-0.09
	90°, Vertical channels	6.2	30.2	6.5	33.2	0.10
Surface coating	$\theta = 18^\circ$ (Uncoated epoxy)	5.7	25.5	6.3	31.2	0.22
	$\theta = 72^\circ$ (Frekote 55-NC)	6.3	31.2	7.9	49.0	0.57
Channel count	4 Channels	6.6	34.2	9.2	66.4	0.94
	8 Channels	6.5	33.2	11.2	98.5	1.97

<sup>a)</sup>Standard sample as previously described; <sup>b)</sup>test conditions conform to the "standard sample" in all respects other than the one specified.

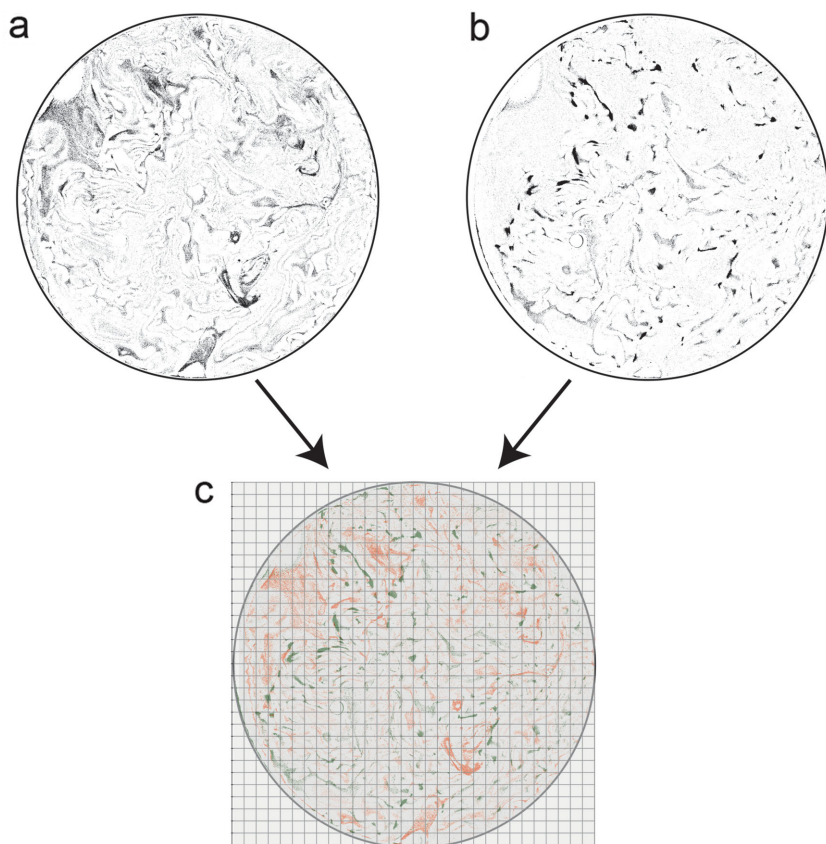


**Figure 8.** Evaluation of mixing from confocal micrographs. a) Binary conversion of rhodamine B (red) channel from Figure 3a (diameter = 6.5 mm). b) Binary conversion of fluorescein (green) channel from Figure 3a. c) Overlaid binary conversion (red = rhodamine B, green = fluorescein) with a representative  $30 \times 30$  grid overlaid. Cell concentrations of each component are calculated and used to determine the Lacey mixing index (Equation (3)). Cells with less than 1.5% concentration of either component were omitted from mixing calculations in order to eliminate empty cells from mixing evaluation.

fill factor for regenerative capabilities of the system, and future studies will lead to systems to better address the challenges related to unpredictable damage orientations and geometries.

#### 4. Experimental Section

**Materials:** Unless otherwise noted, materials were used as received. 2-hydroxyethyl methacrylate (HEMA), dichloroacetic acid (DCA), Luperox DDM-9 (methyl ethyl ketone peroxide solution), cobalt naphthenate, and rhodamine B isothiocyanate (RITC), fluorescein isothiocyanate (FITC), Perylene, and Nile Red were obtained from Sigma Aldrich. 3-aminopropyltriethoxysilane (APS, 99+%) and tetraethoxysilane (TEOS, 99.9+%) were obtained from Gelest. Carbon black (Regal 400) for contrast enhancement was obtained from Cabot Corporation. EPON 828 and Epikure 3230 (Momentive) were obtained from Miller-Stephenson. Frekote NC-55 (Henkel) was obtained from Ellsworth Adhesives. Ultra-Ever Dry was generously provided by Ultratech International Inc. DFWB-K10-50 dye was obtained from Risk Reactor.

**Two-Stage Polymer Solutions:** Syntheses of gelator A, bis-acylhydrazine-terminated poly(ethylene glycol); and gelator B, tris[(4-formylphenoxy)methyl]ethane; were performed following previously described protocols.<sup>[24,25]</sup> The healing chemistry was designed for use as a two-part system requiring gelators to be split between “Part A” and “Part B” solutions. Composition and dyes varied for different experiments, and the formulation of each solution is given in Table S1 in the Supporting

Information. Gelators and HEMA were loaded into scintillation vials and sonicated until dissolved ( $\approx 5$  min). The remaining two-stage components were then added to their respective solution and mixed via vortex mixer. All experiments were performed with solutions containing 12 wt% gelators prepared in quantities commensurate with the number of samples and size of damage to be filled (3–16 mL). Gel times (Table S2, Supporting Information) were determined via inversion of a 10 mm cylindrical vial containing the specified ratio of mixed Part A and B solutions.<sup>[24]</sup> Carbon black was added to HEMA at a concentration of 0.0001 wt% as a contrast agent for visualization in recovery progression experiments and sonicated until well-dispersed. Solutions used for confocal analysis were prepared with HEMA containing (0.1 wt%) fluorescent nanoparticles. Solutions used for fluorescent fill images (Figure 6) were dyed for visualization with  $0.6 \text{ mg mL}^{-1}$  DFWB-K10-50 (Risk Reactor) and  $1.5 \text{ mg mL}^{-1}$  Nile Red in Part B and  $1.25 \text{ mg mL}^{-1}$  perylene in Part A.

**Specimen Fabrication:** Microvascular specimens were fabricated via cell-casting in which silicone gaskets were sandwiched between two glass sheets to create a plate-shaped mold. Fluoropolymer monofilament of  $330 \mu\text{m}$  diameter was suspended between gaskets to create channels  $500 \mu\text{m}$  on center from the top of the specimen. Specimen thickness was controlled by changing the thickness of silicone gasket and microvascular density was controlled by the number and placement of fluoropolymer monofilaments. The mold was filled with epoxy (EPON 828/Epikure 3230) and cured according to manufacturer specifications ( $80 \text{ }^\circ\text{C}$  for 2 h and  $125 \text{ }^\circ\text{C}$  for 3 h). The resulting cured epoxy sheets were removed from the mold, filament extracted by hand, and samples were cut to approximately  $52 \text{ mm} \times 52 \text{ mm}$ . Surface coatings were applied to samples prior to damage using an airbrush (Iwata-Medea Plus C) sprayed at 175 kPa. Cylindrical damage geometries were created using a drill press (RIKON 30-120) with bits of varying diameter to excise a cylindrical plug aligned with the center of the sample.

**Fill Experiments:** Fill experiments were performed under ambient conditions. Part A and B solutions were loaded into 3 mL syringe barrels (Nordson EFD), each split into two syringe tips ( $150 \mu\text{m}$  inner diameter/ $310 \mu\text{m}$  outer diameter, Nordson EFD) with flexible silicone tubing ( $1.59 \text{ mm}$  inner diameter, HelixMark). Syringe tips were inserted into each end of a microchannel. Samples were clamped to keep them stationary and leveled to the appropriate orientation. A small positive pressure was maintained ( $\approx 50 \text{ Pa}$ ) to prevent backflow. Delivery was performed via computer-programmed (LabVIEW 2013) control of pressure dispensers (Ultimus V, Nordson EFD) according to the pump schedules in Figure S2 in the Supporting Information. The delivery rate was held constant at  $3 \mu\text{L min}^{-1}$  per channel for all experiments. Pumping was allowed to continue until either completely filled or failure had occurred by surface wetting, channel blockage, or a lack of detectable progress towards fill over several delivery cycles. Three replicates were performed for each test condition. Graph bars indicate the maximum damage size that all replicates filled and the error bars indicate the maximum damage size that at least 1 of the replicates filled. Overhead images for fill analysis were acquired using a Canon EOS7D DSLR with Canon Macro Lens EF 100 mm 1:2.8 and analyzed using a custom MATLAB (MathWorks) program. The image was thresholded and the outline between filled and unfilled portions of the damage volume was detected and recorded as paired coordinate data. The data from each image was used to construct a best-fit circle which in turn was used to calculate the percent filled and

the circular variance as shown in Equations (1) and (2) and Videos S1 and S2 in the Supporting Information.

**Fluorescent Nanoparticle Synthesis:** Fluorescent nanoparticles were synthesized according to a previously described procedure.<sup>[27,28]</sup> Particle cores containing dye were synthesized by first adding 10 mL ethanol, 0.014 g RITC or 0.012 g FITC, and 0.018 g APS to the reaction vessel and stirring with a magnetic stir bar for 24 h. Next, 115 mL ethanol (200 proof), 6.25 mL ammonium hydroxide (30 wt%), and 40 mL water were added to the reaction vessel. After mixing, 4.5 mL TEOS was added and stirred overnight to complete synthesis of particle cores. Next, a protective shell of silica was grown around the cores in four steps. For each step, a volume of water was added to the reaction vessel followed quickly by an equal volume of TEOS. Between additions, contents were stirred and the reaction vessel was purged with nitrogen. The quantities for each of the four additions were 1, 10, 10, and 10 mL. The total amount of TEOS (31 mL) was chosen to yield an approximate particle diameter of 300 nm with a core diameter of 150 nm. After the particles were synthesized, the contents of the reaction vessel were centrifuged, decanted, and re-dispersed in ethanol three times. The final particle diameter, measured by scanning electron microscope, was approximately 280–350 nm. Particles were stored in ethanol at  $-20^{\circ}\text{C}$  until immediately preceding use. Particles were vacuum-dried and re-dispersed in HEMA via sonication at a concentration of 0.1 wt%.

**Confocal Microscopy and Mixing Analysis:** All samples prepared for confocal microscopy contained a 6.5 mm diameter cylindrical hole. Following the prescribed fill procedure, samples were allowed to cure in a purging nitrogen atmosphere for 24 h before being cut to size, potted (Epofix, Struers), and polished. A sample with perfect mixing was constructed by adding proper ratios of both solutions to a vial, vortex mixing for 5 s, and manually injecting into the damage volume. Confocal fluorescence microscopy was carried out on polished specimens using a laser scanning confocal microscope (LSM 700, Zeiss) with a numerical aperture 0.30 objective (10 $\times$ , 11.2  $\mu\text{m}$  slice) and Zen (Zeiss) software. Samples were analyzed with 485 and 555 nm lasers for fluorescein and rhodamine B containing particles, respectively. A pinhole diameter of 1 Airy unit (AU) was used which yielded a resolution of 1.1  $\mu\text{m}$ . Focal depth was determined at the center of the sample and the depth at which the emission response was at its highest intensity. After setting the focal depth, laser power was adjusted (typically 9–13%) so only a small portion of the fluorescent response achieved maximum intensity. Tile scans were conducted of the entire sample cross-section in an 11  $\times$  11 image array (each 1024  $\times$  1024 pixels) for a total scan time of approximately 60 min per sample. Zen software was further used to process the images by automatically adjusting the brightness and contrast to optimize each image. As shown in Figure 8, ImageJ was used to convert each channel to binary and MATLAB (R2013a) to divide the images into 900-cell grids and calculate cell concentrations of each channel in terms of pixels representing each dye. The cell concentration data was used to calculate the sample mixing ( $n = 3$  for each delivery schedule).

## Supporting Information

Supporting Information is available from the Wiley Online Library or from the author.

## Acknowledgements

This research was financially supported by the Air Force Office of Scientific Research (grant number FA9550-15-1-0087). The authors extend their gratitude to the Beckman Institute and the Institute for Genomic Biology for facilities; E. Jones, graduate student in the Theoretical and Applied Mechanics department for assistance with fluorescent nanoparticle synthesis; and C. Kirk, A. Komnick, and E. Pruitt, undergraduates in the Chemistry department for assistance with two-stage material synthesis.

Received: January 28, 2016

Revised: February 19, 2016

Published online: April 25, 2016

- [1] S. R. White, N. R. Sottos, P. H. Geubelle, J. S. Moore, M. R. Kessler, S. R. Sriram, E. N. Brown, S. Viswanathan, *Nature* **2001**, *409*, 794.
- [2] J. W. C. Pang, I. P. Bond, *Compos. Sci. Technol.* **2005**, *65*, 1791.
- [3] S. J. Kalista, T. C. Ward, Z. Oyetunji, *Mech. Adv. Mater. Struct.* **2007**, *14*, 5.
- [4] D. G. Shchukin, M. Zheludkevich, K. Yasakau, S. Lamaka, M. G. S. Ferreira, H. Mohwald, *Adv. Mater.* **2006**, *18*, 1672.
- [5] E. Palleau, S. Reece, S. C. Desai, M. E. Smith, M. D. Dickey, *Adv. Mater.* **2013**, *25*, 1589.
- [6] S. Neuser, V. Michaud, S. R. White, *Polymer* **2012**, *53*, 370.
- [7] B. J. Blaiszik, S. L. B. Kramer, S. C. Olugebefola, J. S. Moore, N. R. Sottos, S. R. White, *Annu. Rev. Mater. Res.* **2010**, *40*, 179.
- [8] X. Chen, M. A. Dam, K. Ono, A. Mal, H. Shen, S. R. Nutt, K. Sheran, F. Wudl, *Science* **2002**, *295*, 1833.
- [9] P. Cordier, F. Tournilhac, C. Soulie-Ziakovic, L. Leibler, *Nature* **2008**, *451*, 977.
- [10] J. D. Rule, N. R. Sottos, S. R. White, *Polymer* **2007**, *48*, 3520.
- [11] K. S. Toohey, N. R. Sottos, J. A. Lewis, J. S. Moore, S. R. White, *Nat. Mater.* **2007**, *6*, 581.
- [12] H. R. Williams, R. S. Trask, A. C. Knights, E. R. Williams, I. P. Bond, *J. R. Soc. Interface* **2008**, *5*, 735.
- [13] K. S. Toohey, C. J. Hansen, J. A. Lewis, S. R. White, N. R. Sottos, *Adv. Funct. Mater.* **2009**, *19*, 1399.
- [14] C. J. Hansen, W. Wu, K. S. Toohey, N. R. Sottos, S. R. White, J. A. Lewis, *Adv. Mater.* **2009**, *21*, 4143.
- [15] A. R. Hamilton, N. R. Sottos, S. R. White, *Adv. Mater.* **2010**, *22*, 5159.
- [16] C. J. Norris, G. J. Meadway, M. J. O'Sullivan, I. P. Bond, R. S. Trask, *Adv. Funct. Mater.* **2011**, *21*, 362.
- [17] C. J. Hansen, S. R. White, N. R. Sottos, J. A. Lewis, *Adv. Funct. Mater.* **2011**, *27*, 4320.
- [18] A. R. Hamilton, N. R. Sottos, S. R. White, *J. R. Soc. Interface* **2012**, *9*, 1020.
- [19] C. J. Norris, J. A. P. White, G. McCombe, P. Chatterjee, I. P. Bond, R. S. Trask, *Smart Mater. Struct.* **2012**, *21*, 1.
- [20] J. F. Patrick, K. R. Hart, B. P. Krull, C. E. Diesendruck, J. S. Moore, S. R. White, N. R. Sottos, *Adv. Mater.* **2014**, *26*, 25.
- [21] X. Zhu, Z. Zhang, X. Men, J. Yang, K. Wang, X. Xu, X. Zhou, Q. Xue, *J. Mater. Chem.* **2011**, *21*, 15793.
- [22] X. Yong, O. Kuksenok, K. Matyjaszewski, A. C. Balazs, *Nano Lett.* **2013**, *13*, 6269.
- [23] S. Zavada, N. McHardy, K. Gordon, T. Scott, *ACS Macro Lett.* **2015**, *4*, 819.
- [24] S. White, J. Moore, N. Sottos, B. Krull, W. Santa Cruz, R. Gergely, *Science* **2014**, *344*, 620.
- [25] G. Deng, C. Tang, F. Li, H. Jiang, Y. Chen, *Macromolecules* **2010**, *43*, 1191.
- [26] I. Kasa, *IEEE Trans Instrum. Meas.* **1976**, *IM-25*, 1.
- [27] A. Van Blaaderen, A. Vrij, *Langmuir* **1992**, *8*, 2921.
- [28] N. A. M. Verhaegh, A. Van Blaaderen, *Langmuir* **1994**, *10*, 1427.
- [29] P. M. C. Lacey, *J. Appl. Chem.* **1954**, *4*, 257.
- [30] J. F. Oliver, C. Huh, S. G. Mason, *J. Colloid Interface Sci.* **1977**, *59*, 3.
- [31] B. P. Casavant, E. Berthier, A. B. Theberge, J. Berthier, S. I. Montanez-Sauri, L. L. Bischel, K. Brakke, C. J. Hedman, W. Bushman, N. P. Keller, D. J. Beebe, *Proc. Natl. Acad. Sci. USA* **2013**, *110*, 25.
- [32] Z. Xue, M. Liu, L. Jiang, *J. Polym. Sci. Part B Polym. Phys.* **2012**, *50*, 1209.